



This is a repository copy of *Compositional transformation and impurity-mediated optical transitions in co-evaporated Cu₂AgBiI₆ thin films for photovoltaic applications*.

White Rose Research Online URL for this paper:

<https://eprints.whiterose.ac.uk/208099/>

Version: Published Version

Article:

Putland, B.W.J., Righetto, M. orcid.org/0000-0001-5507-1445, Jin, H. orcid.org/0000-0002-4372-897X et al. (6 more authors) (2024) Compositional transformation and impurity-mediated optical transitions in co-evaporated Cu₂AgBiI₆ thin films for photovoltaic applications. *Advanced Energy Materials*. ISSN 1614-6832

<https://doi.org/10.1002/aenm.202303313>

Reuse

This article is distributed under the terms of the Creative Commons Attribution (CC BY) licence. This licence allows you to distribute, remix, tweak, and build upon the work, even commercially, as long as you credit the authors for the original work. More information and the full terms of the licence here:

<https://creativecommons.org/licenses/>

Takedown

If you consider content in White Rose Research Online to be in breach of UK law, please notify us by emailing eprints@whiterose.ac.uk including the URL of the record and the reason for the withdrawal request.



eprints@whiterose.ac.uk
<https://eprints.whiterose.ac.uk/>

Compositional Transformation and Impurity-Mediated Optical Transitions in Co-Evaporated $\text{Cu}_2\text{AgBiI}_6$ Thin Films for Photovoltaic Applications


Benjamin W. J. Putland, Marcello Righetto, Heon Jin, Markus Fischer, Alexandra J. Ramadan, Karl-Augustin Zaininger, Laura M. Herz,* Harry C. Sansom,* and Henry J. Snaith*

Quaternary copper-silver-bismuth-iodide compounds represent a promising new class of wide-bandgap (2 eV) semiconductors for photovoltaic and photodetector applications. In this study, vapor phase co-evaporation is utilized to fabricate $\text{Cu}_2\text{AgBiI}_6$ thin films and photovoltaic devices. The findings show that the properties of vapor-deposited films are highly dependent upon processing temperature, exhibiting increased pinhole density and transforming into a mixture of quaternary, binary, and metallic phases depending on the post-deposition annealing temperature. This change in phase is accompanied by an enhancement in photoluminescence (PL) intensity and charge-carrier lifetime, along with the emergence of an additional absorption peak at high energy (≈ 3 eV). Generally, increased PL is a desirable property for a solar absorber material, but this change in PL is ascribed to the formation of CuI impurity domains, whose defect-mediated optical transition dominates the emission properties of the thin film. Via optical pump terahertz probe spectroscopy, it is revealed that CuI impurities hinder charge-carrier transport in $\text{Cu}_2\text{AgBiI}_6$ thin films. It is also revealed that the predominant performance limitation in $\text{Cu}_2\text{AgBiI}_6$ materials is the short electron-diffusion length. Overall, the findings pave the way for potential solutions to critical issues in copper-silver-bismuth-iodide materials and indicate strategies to develop environmentally compatible wide-bandgap semiconductors.

1. Introduction

Realizing affordable utility-scale multi-junction solar cells would represent a fundamental shift in the photovoltaic (PV) landscape by reducing the levelized cost of electricity beyond that attainable using single-junction modules, and reducing required land use.^[1–3] Typically, for triple-junction cells incorporating silicon as the base absorber (E_g 1.1 eV), the optimum bandgap of the top cell is 1.95 eV, whilst for “all perovskite” multi-junctions utilizing a 1.22 eV Pb-Sn based absorber, the ideal top cell is 2.04 eV.^[4] The development of highly efficient intrinsic wide-bandgap semiconductors is therefore critical. The versatility of the ABX_3 ($A = \text{Cs}^+$, FA^+ , $B = \text{Pb}^{2+}$, $X = \text{I}^-$, Br^-) perovskite structure makes hybrid lead-halide materials of particular interest. The ability to tune their bandgap by alloying iodide with bromide sustains many of the excellent optoelectronic properties associated with the $[\text{PbI}_6]^{+}$ octahedral framework in lower bandgap

B. W. J. Putland, M. Righetto, H. Jin, M. Fischer, A. J. Ramadan, K.-A. Zaininger, L. M. Herz, H. C. Sansom, H. J. Snaith
Department of Physics, University of Oxford
Clarendon Laboratory
Parks Road, Oxford OX1 3PU, UK
E-mail: laura.herz@physics.ox.ac.uk; harry.sansom@physics.ox.ac.uk; henry.snaith@physics.ox.ac.uk

 The ORCID identification number(s) for the author(s) of this article can be found under <https://doi.org/10.1002/aenm.202303313>

© 2024 The Authors. Advanced Energy Materials published by Wiley-VCH GmbH. This is an open access article under the terms of the [Creative Commons Attribution](https://creativecommons.org/licenses/by/4.0/) License, which permits use, distribution and reproduction in any medium, provided the original work is properly cited.

DOI: 10.1002/aenm.202303313

M. Fischer
Institute of Electromagnetic Fields
ETH Zurich
Gloriastrasse 35, Zurich 8092, Switzerland
A. J. Ramadan
Department of Physics & Astronomy, University of Sheffield
Hicks Building
Hounsfield Road, Sheffield S3 7RH, UK
L. M. Herz
Institute for Advanced Study
Technical University of Munich
Lichtenbergstrasse 2a, D-85748 Garching, Germany

perovskites, that is, strong optical absorption, long charge-carrier diffusion lengths, and long charge-carrier lifetimes.^[5–8] However, bromide-rich mixed-halide perovskites are usually unstable under illumination, reversibly segregating into iodide- and bromide-rich regions leading to funneling of photo-excited charges across compositionally heterogeneous regions.^[9,10] This, coupled with the low thermal stability of the organic cation, makes all inorganic, single-halide absorber materials preferable.^[11,12] A vast majority of such materials are centered on alternating [AgX₆] and [BiX₆] (X = I[−], Br[−], Cl[−]) octahedral networks. The corner-sharing double perovskites, in particular Cs₂AgBiBr₆, have been studied because of their preferred high stability and microsecond charge-carrier lifetimes.^[13–15] Nevertheless, power conversion efficiencies (PCEs) of photovoltaic devices have been slow to progress as a result of a combination of small electron diffusion lengths and the large absorber thickness made necessary by the weakly absorbing indirect bandgap (1.8–2.2 eV) of the material.^[16–19] Alternatively, several edge-sharing ternary silver bismuth iodide compositions (Ag_xBi_yI_{x+3y}) have been shown to possess encouraging photovoltaic properties and, importantly, direct bandgaps around 1.8–2 eV^[20–24]—of which the silver-rich Ag₂BiI₅ and Ag₃BiI₆ compositions have systematically outperformed AgBiI₄ and AgBi₂I₇ in photovoltaic devices, with the record PCE (5.56%) reported for sulfur-doped Ag₃BiI_{5,92}S_{0.04}.^[25] Despite positive advancements, low short-circuit current density and radiative efficiency,^[20,26,27] film processing issues,^[28,29] and Ag⁺ migration have all been reported.^[30] More recently, Sansom et al. expanded the Ag-Bi-I phase space through incorporation of monovalent Cu⁺, discovering two novel quaternary Cu-Ag-Bi-I (sometimes referred to as CABI) absorbers: CuAgBiI₅ and Cu₂AgBiI₆. Initial studies showed Cu₂AgBiI₆ has a direct 2.06 eV bandgap suitable for tandems and triple junctions, a high absorption coefficient comparable to the best-in-class perovskites (≈10⁵ cm^{−1}), as well as modest yet promising 0.43% PCE.^[31] The role of Cu⁺ is crucial in enhancing electronic orbital connectivity between otherwise electronically isolated silver and bismuth octahedra (i.e., increasing the so-called electronic dimensionality of the material),^[32] leading to improved charge transport via increased mobility and reduced exciton binding energy.^[33] This enhanced transport is attributed to Cu⁺ contributing to the density of states at the top of the valence band.^[31,33] A shallower valence band maximum (VBM) also has the further advantage of more favorable band alignment between Cu₂AgBiI₆ (−5.21 eV),^[31] and typical hole transport layers such as poly[bis(4-phenyl)(2,4,6-trimethylphenyl)amine] PTAA (−5.2 eV),^[34] 2,2',7,7'-tetrakis(N,N-di-*p*-methoxy-phenylamine)-9,9'-spirobifluorene (Spiro-OMeTAD) (−5.2 eV),^[35] and NiO (−5.2 eV),^[36] in comparison to the valence band maximum of the silver bismuth iodides (≈−5.6–5.9 eV).^[22,28,37] Cu₂AgBiI₆ has since been developed for use as photodetectors,^[38] and in solar cells under both AM1.5 and indoor irradiation spectrums.^[39–42]

Studies on Cu₂AgBiI₆ have so far all been conducted on solution-processed thin films or powder samples. Due to phase heterogeneity, poor morphology, low crystallinity, and low precursor solubility, formative investigations have concentrated on optimizing the deposition process. This has either been through additive or solvent engineering such as mixing dimethyl sulfoxide (DMSO) with the heterocyclic organic compound pyridine, or in-

corporation of phenethylammonium iodide (PEAI) or hydroiodic acid (HI), which proves effective in passivating surface defects and improving the crystallization and grain structure.^[38,39,43] Despite the use of deposition engineering techniques such as gas and anti-solvent quenching, ink optimization, hot-casting, and two-step annealing, their efficacy has not been as pronounced as they have been for lead-halide perovskites. The influence of the deposition method on Cu₂AgBiI₆ film quality, particularly in the context of phase heterogeneity and high pinhole density when the optimal solution/spin-coating conditions are not met, was recently highlighted by Pai et al.,^[42] These stringent processing requirements pose a challenge for optimizing the crystallization process, which limits the options for controlling the grain size and thickness, reducing the defect density, and ultimately enhancing the PCE through deposition engineering.

Another challenge associated with Cu₂AgBiI₆ materials is charge transport and consequently low extracted current density. Optical pump terahertz probe (OPTP) measurements reveal strong charge-lattice interactions.^[44] Photoconductivity transients show a fast decay (on the order of picoseconds) of the initial photoconductivity signal followed by a long-lived signal component. Buizza et al. demonstrated how this is typical of charge-carrier localization, causing an initially delocalized large polaron to localize and form a small polaron whose mobility is significantly reduced compared to the delocalized state, contributing to low drift and diffusion rates.^[44] Second, non-radiative recombination loss mechanisms such as point defects are important to consider because they act as charge traps that reduce current, which may also explain the low photoluminescence intensity and open-circuit voltages found thus far in Cu₂AgBiI₆ materials and solar cells. Such traps have been attributed to iodine vacancies, facilitated by the highly disordered Cu₂AgBiI₆ structure.^[40] Partial substitution of bismuth (III) for antimony (III) was shown to be effective in reducing the lattice disorder and formation energy of intrinsic defects. For example, when exposed to “indoor” illumination using a 1000 lux white light-emitting diode, Cu₂AgBiI₆-Sb photovoltaic devices achieved nearly double the PCE of the nominal Cu₂AgBiI₆ absorber, increasing from 5.52% to 9.53%.^[40] Under AM1.5G radiation, the champion PCE reported for the nominal Cu₂AgBiI₆ is currently 2.39% and exhibits notable stability of up to 240 days in ambient conditions.^[42] However, up to this point, the most efficient Cu₂AgBiI₆ devices have consistently employed a mesoporous electron-transport layer. In contrast, planar heterojunction device architectures have faced challenges in surpassing 1% efficiency, primarily due to limitations in current density. Nevertheless, these encouraging characteristics call for further development and a deeper understanding of these newly emerged Cu₂AgBiI₆ materials.

The utilization of thermal evaporation for the absorber in photovoltaic devices has gained popularity due to its scalability. This approach could be particularly advantageous for Cu₂AgBiI₆ materials, given the strict processing conditions we previously described. Thermal evaporation provides a wider parameter space for investigation, such as varying thicknesses, annealing pre- and post-deposition, and different compositions, without the need to optimize a multitude of solution-coating variables, while still maintaining conformal coverage. Despite these benefits, no studies have yet explored the potential of vapor-deposited Cu₂AgBiI₆. In this study, we demonstrate the use of multi-source

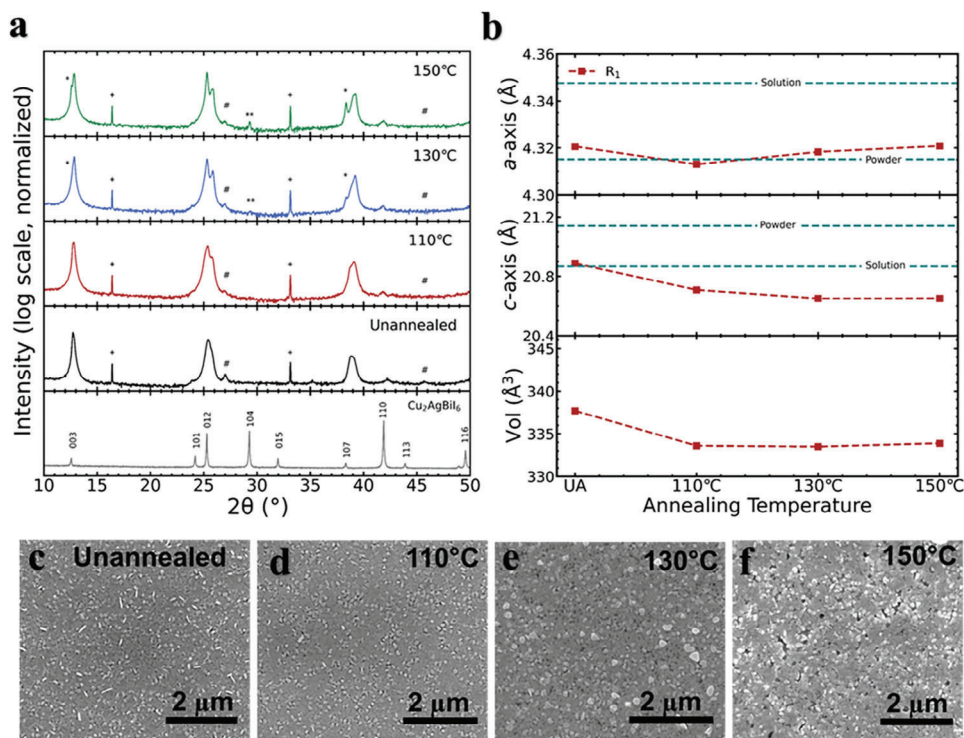


Figure 1. a) Experimental X-ray diffraction patterns of unannealed and annealed Cu₂AgBi₆ films (in air) using Cu-K α as the radiation source. Unannealed, 110, 130, and 150 °C annealed films all refine to a single rhombohedral Cu₂AgBi₆ phase (space group $R\bar{3}m$),^[31] but with varying impurity constitutions. Impurity peaks belonging to BiI₃, CuI, and metallic bismuth are marked with (#), (*), and (**), respectively. Reflections from the quartz substrate are marked with (+). b) Lattice constants and unit cell volume (taken from Table S1, Supporting Information) of the evaporated Cu₂AgBi₆ unit cell, R_1 (red dashed line), as a function of annealing temperature. Unit cell lattice parameters of powder and solution-processed thin films of Cu₂AgBi₆ reported in literature are plotted for reference (teal dashed line).^[31] Top-view scanning electron microscopy images of c) unannealed films, and d) 110 °C, e) 130 °C, and f) 150 °C annealed Cu₂AgBi₆ films.

co-evaporation to fabricate polycrystalline Cu₂AgBi₆ films and devices. We carry out a detailed phase, morphology, and optoelectronic analysis to investigate how the structural and optoelectronic properties change following a range of annealing temperatures, and in doing so, identify several performance limiting factors of key importance to the advancement of Cu₂AgBi₆.

2. Results

We prepare 250 nm thick Cu₂AgBi₆ films by co-evaporating CuI, AgI, and BiI₃ separately under vacuum (10⁻⁶ mbar) using three resistively heated sources. All precursor powders readily evaporate at temperatures less than 500 °C. Tuning the evaporation rates of each source attains an average composition of Cu_{2.12(12)}Ag_{1.04(18)}Bi_{0.95(7)}I_{6.00(14)}, as characterized by scanning electron microscopy energy dispersive X-ray spectroscopy (SEM-EDX), which is within 1 σ error of the nominal target composition, Cu₂AgBi₆. The numbers in brackets represent the error, calculated as the standard deviation of at least 6 SEM-EDX measurements. A detailed fabrication procedure is outlined in the Supporting Information. We also highlight an unforeseen synthetic challenge in evaporating AgI, which depends on the choice of crucible material. We describe it in the Supporting Information and Figure S3, Supporting Information, but note here that using an opaque crucible, such as alumina (Al₂O₃), is important.

2.1. Phase Description and Film Morphology

To gain insight into the deposited phases, we carry out X-ray diffraction (XRD) measurements and conduct phase identification and unit cell analysis using Pawley fitting. The XRD data of unannealed films is shown in Figure 1a. The crystal structure refines to a single trigonal phase (space group $R\bar{3}m$) with $a = b = 4.3206(8)$ Å, $c = 20.888(8)$ Å. Whilst the space group is consistent with literature reports, in our evaporated films a and c axes are larger and smaller, respectively, than those measured for Cu₂AgBi₆ powder synthesized via solid-state reactions at high temperature ($a = b = 4.3151(2)$ Å, $c = 21.141(1)$ Å), but similar to the lattice parameters of solution-processed films ($a = b = 4.3476(8)$ Å, $c = 20.80(1)$ Å).^[31] Small impurity peaks belonging to BiI₃ are also observed (marked (#) in Figure 1a). Compared to the random orientation of powdered Cu₂AgBi₆,^[31] and solution-processed Cu₂AgBi₆,^[31,40,41] the relative intensities of the Bragg reflections indicate unannealed evaporated films favor out-of-plane growth along the [003] direction.

Though not always necessary, evaporated metal halide films are often annealed post-deposition to enhance phase purity, crystallinity, and morphology,^[20,45,46] which could be important for evaporated Cu₂AgBi₆ considering films are multiphase. Scanning electron microscopy (SEM) of unannealed films (Figure 1c) also reveals small grains (≈ 50 –100 nm), pinholes, and rod-like

impurities likely to be BiI₃, consistent with the low-intensity BiI₃ peaks observed in XRD measurements, and the morphology of our evaporated neat BiI₃ films (Figure S4a, Supporting Information). For these reasons, we anneal films post-deposition for 15 min in air between 110 and 150 °C and measure the surface morphology, composition, and phase constitution using a combination of SEM, SEM-EDX, XRD, and Pawley fittings. The diffraction patterns are presented in Figure 1a. The fits, and a detailed unit cell and compositional analysis are presented in Figure S5 and Table S1, Supporting Information, respectively. To summarize, we fit all annealed films to a single rhombohedral phase (space group $R\bar{3}m$) with varying lattice parameters and impurity constitution. Films annealed at 110 °C have an average composition of Cu_{2.12(12)}Ag_{1.18(11)}Bi_{1.07(15)}I_{6.00(10)} and are fitted to a single trigonal phase, R_1 , with lattice parameters $a = b = 4.313(1)$ Å, $c = 20.709(4)$ Å (space group $R\bar{3}m$). Films annealed at 130 °C have an average composition of Cu_{2.05(19)}Ag_{1.21(16)}Bi_{1.09(10)}I_{6.00(24)}, and are fitted to a trigonal unit cell, R_1 , with lattice parameters $a = b = 4.3183(3)$ Å, $c = 20.651(2)$ Å. Films annealed at 150 °C have an average composition of Cu_{2.03(20)}Ag_{1.07(9)}Bi_{1.14(7)}I_{6.00(23)} and are fitted with a trigonal unit cell, R_1 , with lattice parameters $a = b = 4.3208(1)$ Å, $c = 20.6519(6)$ Å. The composition of all annealed films are within 1 σ error of the composition measured for unannealed films, indicating no preferential loss of elements within the sensitivity of SEM-EDX over the investigated temperature range. We do not observe XRD peaks belonging to common oxides or oxyhalides (e.g., BiOI, CuO, Cu₂O, or Ag₂O) that may form as a result of annealing in air. Similar to unannealed films, we identify the ever presence of BiI₃ impurity peaks in the annealed films. Unlike for unannealed films, we identify peaks belonging to CuI (marked (*), Figure 1a) in films annealed at 110, 130, and 150 °C, which increase in intensity with annealing temperature. We assign these peaks to a previously reported^[47] trigonal CuI unit cell (space group $P3m1$: Coll.Code: 30363, ICSD database), with lattice parameters $a = b = 4.355(1)$ Å, $c = 20.853(8)$ Å. This trigonal CuI phase has similar lattice parameters to the main quaternary Cu₂AgBiI₆ phase, thereby potentially explaining the preferential formation over the cubic zinc blende structure. Owing to the overlapping XRD peaks of CuI and Cu₂AgBiI₆ phases, it is difficult to infer the effect that annealing has on crystallinity of the main Cu₂AgBiI₆ phase, R_1 . XRD data also shows that films annealed at 130 and 150 °C contain metallic bismuth (**), which is consistent with the satellite peaks found in the bismuth 4f spectra as measured by X-ray photoelectron emission spectroscopy (Figure S6, Supporting Information), and observations reported for solution-processed films.^[42] We gain insight into main Cu₂AgBiI₆ phase, R_1 , by analyzing the evolution of lattice parameters with temperature, as shown in Figure 1b. Here, as the annealing temperature increases, the a -axis and unit cell volume of R_1 initially decrease, then increase for films annealed at 130 and 150 °C. The c -axis, however, monotonically decreases with temperature, with the largest decrease observed during the unannealed to 110 °C annealed state. We argue that these changes are caused by the changing composition of the main phase and/or impurity constitution, that is, loss of tetrahedral Cu⁺ and octahedral Bi³⁺. However, given we do not see a clear discontinuity in the a and c lattice parameters, we infer R_1 remains structurally 2D, as opposed to transitioning to the 3D octahedral network associated with CuAgBiI₅.^[33]

To assess the evolution of morphology across the investigated temperature range, we compare top-view SEM of unannealed and annealed films, as shown in Figure 1c–f. In agreement with XRD analysis and similar to unannealed films, we identify BiI₃ impurity grains in all annealed films. Films annealed at 110 °C remain largely unchanged from unannealed films, but temperatures of 130 and 150 °C cause the films to develop surface features and to visibly degrade through increasing pinhole density and size with temperature. Considering the impurity constitution as identified by XRD and the typical morphology of evaporated pure CuI films (Figure S4b, Supporting Information), we speculate the surface features to be CuI, rather than Bi⁰ agglomerates.

2.2. Optoelectronic Properties

To probe the conductivity and doping, we compared the long-range in-plane electrical conductivity of evaporated unannealed and 150 °C annealed films to solution-processed Cu₂AgBiI₆ films, using measurements obtained via the Van der Pauw method.^[50] In this four-point square configuration, a current is applied across two contacts, and the voltage is measured between the remaining two opposite contacts. A full description of the sample layout and measurement procedure is included in the Supporting Information (Figure S7, Supporting Information). The results are shown in Figure 2a. Interestingly, we measure the conductivity of unannealed evaporated Cu₂AgBiI₆ films to be $(2 \pm 1) \times 10^{-2}$ S cm⁻¹, which is several orders of magnitude greater than that of the 150 °C annealed films $((5 \pm 3) \times 10^{-5}$ S cm⁻¹) and solution-processed Cu₂AgBiI₆ films $((1.2 \pm 0.2) \times 10^{-5}$ S cm⁻¹). Whilst the conductivities for evaporated annealed and solution-processed Cu₂AgBiI₆ are similar to values reported for MAPI and double and triple-cation (FA:MA:Cs) perovskites,^[51] the conductivity of unannealed films is high, indicating high free charge-carrier doping density. On the same plot, we show the associated free charge-carrier densities, calculated from the conductivity (σ) and localized-state charge-carrier mobility (μ_{loc}) values (which we will discuss in more detail below). Evaporated unannealed Cu₂AgBiI₆ films have the highest free charge-carrier density of 9.6×10^{16} cm⁻², followed by 150 °C annealed (2.8×10^{14} cm⁻²), and solution-processed (8.9×10^{13} cm⁻²) films. The observed trend indicates that the unintentional “doping density” is strongly dependent upon annealing temperature and processing methodology. The origin of the change in apparent p-doping and conductivity with annealing temperature is subject to ongoing investigations.

We investigate the electronic band structure and estimate the VBM of evaporated films using ultraviolet photoelectron spectroscopy (UPS). The results are shown in Figure 2b. The VBM (E_v) of unannealed films is measured to be -5.2 eV, consistent with Cu₂AgBiI₆ powder (-5.21 eV).^[31] The work function (Fermi level, E_f) is measured to be -4.0 eV, and by adding the optical bandgap to the VBM ($E_v + E_g$), we infer the conduction band minimum (CBM) to be -3.1 eV, which compares to literature values of -3.15 eV for bulk Cu₂AgBiI₆ powder,^[31] and -3.36 ^[42] and -3.83 eV,^[38] for solution-processed films. Measurements of annealed films show a monotonic deepening of the VBM, from -5.2 to -5.3 eV, and -5.5 eV for unannealed, 130, and 150 °C annealed films, respectively. The Fermi level also deepens

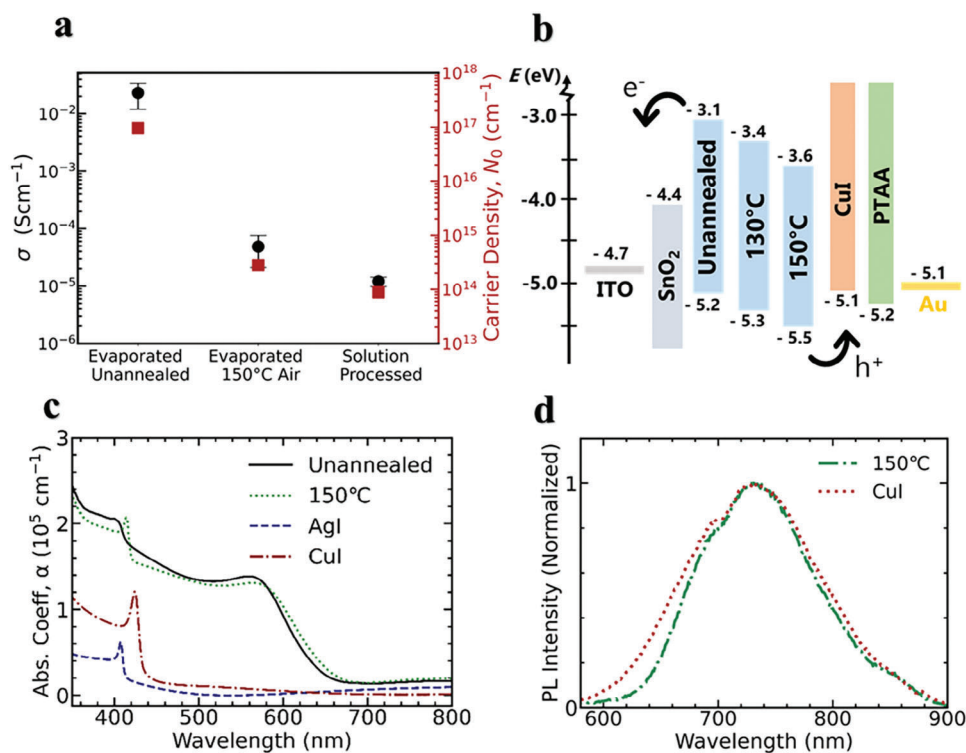


Figure 2. a) Electrical conductivity and corresponding inferred charge-carrier density of evaporated and solution-processed Cu₂AgBiI₆ films. The error bars illustrate the standard deviation in conductivity observed among five samples. b) Schematic band alignment of valence and conduction band energies of evaporated Cu₂AgBiI₆ films, electron transport layer SnO₂, CuI, electrodes (Au, indium tin oxide (ITO)), and the HOMO of the hole transport layer poly[bis(4-phenyl)(2,4,6-trimethylphenyl)amine] (PTAA) used in photovoltaic devices. The energy levels of the Cu₂AgBiI₆ films were measured using ultraviolet photoelectron spectroscopy (UPS), whilst values for the transport layers were taken from literature.^[34,48,49] c) Absorption coefficient of multiphase unannealed and annealed Cu₂AgBiI₆ films and evaporated 300 nm thick CuI and AgI films. d) Steady-state photoluminescence spectroscopy showing evaporated Cu₂AgBiI₆ films annealed at 150 °C strongly overlap with a defect-mediated optical transition found in CuI films.

relative to unannealed films, from -4.0 to -4.3 eV and -4.3 eV, respectively. This behavior can be explained by considering the role that Cu⁺ plays in contributing to the band structure of Cu-Ag-Bi-I compounds.^[31,33] Increased Cu⁺ is associated with a shallower VBM and CBM, and narrower bandgap.^[31] As a result, compositions containing greater Cu⁺ such as Cu₂AgBiI₆ have a shallower VBM (≈ -5.2 eV) compared to CuAgBiI₅ (-5.47 eV), and the ternary silver bismuth iodides (≈ -5.6 – -5.9 eV).^[22,28,37] We therefore infer that the loss of tetrahedral Cu⁺ from the quaternary structure during annealing, in the form of CuI impurity domains, is responsible for the changes in band structure we observe, as supported by our XRD and SEM measurements. This is further consistent with PL and absorption measurements described below.

To probe the absorption properties of unannealed and annealed Cu₂AgBiI₆ films, we measure the ultraviolet-visible (UV-Vis) absorption spectra and calculate the absorption coefficient, α , as a function of wavelength, as shown in Figure S8a, Supporting Information. The absorption onset and profile are typical of that observed for Cu₂AgBiI₆.^[39] All films display strong absorption in the visible region and a red shift in absorption onset with increasing temperature. To account for the excitonic contribution to the continuum of states, we model the experimental absorption coefficient following the theory developed by Elliott^[44,52] (Figure S9a–d, Supporting Information) and

estimate a direct bandgap of unannealed films to be 2.13 eV, which is marginally larger but consistent with 2.06 eV reported for solution-processed Cu₂AgBiI₆.^[31] As reported in Table S2, Supporting Information, the bandgap decreases upon annealing, with 110, 130, and 150 °C annealed films showing reduced bandgaps of 2.09–2.10 eV. Furthermore, the fitting also confirms the exciton binding energy to be largely unchanged (17–24 meV) over the temperature range, and comparable to room temperature thermal energies (≈ 26 meV) and those reported for solution-processed Cu₂AgBiI₆.^[31,44]

A key feature of the absorption profile of evaporated Cu₂AgBiI₆, which has also been observed in solution-processed Cu₂AgBiI₆ materials,^[38,39] is the emergence of an absorption peak at ≈ 415 nm. In evaporated films, this peak redshifts from 408 nm for unannealed films, to 411, 414, and 417 nm for 110, 130, and 150 °C annealed films, respectively. Upon annealing to 130 and 150 °C, the peak becomes noticeably sharper. Although Grandhi et al. reported a similar observation for HI-treated solution-processed Cu₂AgBiI₆,^[39] the origin has not yet been clarified. While Grandhi et al. suggested it could originate from AgI, BiI₃, or Cu₂BiI₅ impurities, we assign this feature to a CuI-rich impurity. As shown in Figure 2c, the absorption edge of CuI is very close to the additional absorption edge observed in Cu₂AgBiI₆ films. However, since the absorption peak exists between those of AgI and CuI, it is also possible that the phase

is a mixed $\text{Cu}_{1-x}\text{Ag}_x\text{I}$ impurity, which commonly crystallizes in a cubic or hexagonal structure.^[53] Nevertheless, the lattice parameters we identify for the impurity phase in these evaporated $\text{Cu}_2\text{AgBiI}_6$ materials are $a = b = 4.355(1) \text{ \AA}$, $c = 20.853(7) \text{ \AA}$ (space group P3m1). This is very close to the values obtained for a known polymorph of CuI.^[47,54] We therefore believe that if Ag^+ is present in the structure, the phase is likely a Cu-rich $\text{Cu}_x\text{Ag}_{1-x}\text{I}$ phase. This assignment is further corroborated by photoluminescence measurements. As shown in Figure S8b, Supporting Information for the $\text{Cu}_2\text{AgBiI}_6$ films, we observe strong PL emission between 720 and 760 nm following 405 nm excitation, with PL intensity increasing and blue shifting, and full width at half maximum (FWHM) narrowing, with annealing temperature. However, similar to Grandhi et al. we find that photoluminescence emission is strongly dependent on excitation energy. We could not detect any PL signal following excitation from 510 or 635 nm (Figure S8d, Supporting Information). Interestingly, the emission from annealed $\text{Cu}_2\text{AgBiI}_6$ films matches very well with the CuI defect emission band (Figure 2d), with all spectra peaking near 730 nm.^[55–57] Since photoexcitation laser energies above the $\text{Cu}_2\text{AgBiI}_6$ absorption onset but lower than the CuI one do not result in observable emission, but laser excitation energies above the CuI band gap do result in PL, it appears that the PL from $\text{Cu}_2\text{AgBiI}_6$ is predominantly originating from the defect band in the impurity, rather than the band-to-band transition in $\text{Cu}_2\text{AgBiI}_6$. This defect emission from CuI has been previously assigned to electron traps (I^- vacancies) in CuI.^[56,58] Based on the expected relative band alignment, CuI embedded in $\text{Cu}_2\text{AgBiI}_6$ films will form a heterojunction (Figure 2b). Specifically, CuI (-5.2 eV) and $\text{Cu}_2\text{AgBiI}_6$ (-5.2 eV) valence band edges are close in energy. On the other hand, reported conduction band onsets for $\text{Cu}_2\text{AgBiI}_6$ (-3.35 eV)^[42] suggests a lower-lying conduction band with respect to that of CuI (-2.1 eV).^[59] Consequently, upon high energy excitation, we expect holes to diffuse freely between CuI and $\text{Cu}_2\text{AgBiI}_6$, whereas electrons should be preferentially funneled to $\text{Cu}_2\text{AgBiI}_6$ unless they are trapped at I^- vacancy defects in CuI. Given this band alignment, freely diffusing holes can promote radiative recombination at CuI defect sites where electrons are likely to become trapped. The enhanced PL and CuI XRD peak intensity are consistent with the increased quantity of CuI in the films upon higher temperature annealing. We also observe longer PL lifetimes with increasing annealing temperature as shown in Figure S8c, Supporting Information. The increased PL lifetime is unexpected and raises the question of possible interactions between CuI defects and charge carriers in the $\text{Cu}_2\text{AgBiI}_6$.

Additionally, we compare unannealed and air-annealed films with films that have been annealed in I_2 -vapor at $150 \text{ }^\circ\text{C}$ (hereon labeled “treated”). I_2 -vapor annealing has been demonstrated as an effective strategy to passivate iodine defects in CuI, quenching the defect-mediated transition and thus potentially reducing the possibility of electrons transferring from $\text{Cu}_2\text{AgBiI}_6$ to CuI via the defect state.^[55] The I_2 -annealing procedure and its impact on the phase, morphology, and optoelectronic properties (Figure S10, Supporting Information) are described in the Supporting Information. To summarize, Pawley fitting of XRD data (Figure S10h, Supporting Information) suggests the phase constitution remains largely unchanged from films annealed in air. Both films contain BiI_3 impurities, metallic bismuth, and CuI impurities.

However, XRD peaks belonging to CuI were more intense in I_2 -vapor annealed samples (Figure S10a, Supporting Information). This is reflected in photoluminescence and absorption measurements, where films annealed in I_2 vapor absorb more strongly at the CuI band edge (Figure S10b, Supporting Information), are more luminescent (Figure S10c, Supporting Information), and show longer photoluminescence decay lifetime (Figure S10d, Supporting Information). The morphology (Figure S10g, Supporting Information) of treated films also contained more abundant CuI surface species, in addition to greater pinhole density.

We emphasize here the significance of our findings concerning the CuI defect band emission. Photoluminescence is widely used as a metric to quantify the quality of solar absorber materials. This approach is valid only when PL originates from the band-to-band transition: in this case, increases in PL intensity and lifetime indicate reduced non-radiative recombination (e.g., charge-carrier trapping) and therefore reduced defect densities. However, when the PL originates from a defect state, as appears to be the case here, intense PL emission and long PL lifetimes indicate increased charge-carrier trapping at the defect sites. Therefore, the presence of the defect band emission is indicative of a sub-optimal material and imposes careful considerations in the assessment of PL from emerging solar absorbers. This could also suggest that we have not yet measured and determined the band-to-band emission properties of $\text{Cu}_2\text{AgBiI}_6$. However, it is also possible that the band-edge PL of $\text{Cu}_2\text{AgBiI}_6$ falls within the same spectral window as the CuI defect emission, which further complicates matters.

Given the prominent role played by CuI in annealed $\text{Cu}_2\text{AgBiI}_6$ thin films and its possible implications on $\text{Cu}_2\text{AgBiI}_6$ solar cell operation, we investigate the effects of the presence of CuI in $\text{Cu}_2\text{AgBiI}_6$ films on the charge-carrier dynamics using optical-pump-terahertz-probe (OPTP) spectroscopy. By measuring the fractional change in transmitted THz electric-field amplitude (expressed here as $-\Delta T/T$) upon photoexcitation, this technique monitors changes in the photoconductivity of the material, giving insight into the dynamics of photo-generated free charge carriers. To disentangle the effect of CuI domains on the charge-carrier dynamics in $\text{Cu}_2\text{AgBiI}_6$ films, we used two different photoexcitation wavelengths: 400 nm excitation to directly excite both CuI and $\text{Cu}_2\text{AgBiI}_6$ domains, and 520 nm excitation to excite charge carriers in $\text{Cu}_2\text{AgBiI}_6$ selectively. OPTP photoconductivity transients measured following 520 nm (i.e., selective $\text{Cu}_2\text{AgBiI}_6$ excitation) and 400 nm excitation for unannealed, air-annealed, and I_2 -annealed $\text{Cu}_2\text{AgBiI}_6$ thin films are shown in Figure 3a,b. Photoconductivity transients for all the measured thin films show qualitatively similar behavior, featuring a fast decay of the initial photoconductivity signal followed by a long-lived signal component. Buizza et al. previously demonstrated how charge-carrier localization causes a rapid initial decay of the photoconductivity in $\text{Cu}_2\text{AgBiI}_6$.^[33,44] Here, delocalized large polarons generated after photoexcitation rapidly localize to form small polarons, with the mobility of the large polarons estimated by the peak in the photoconductivity.^[44] To quantitatively interpret the effect of this localization, Wright et al. and Buizza et al. developed a two-level mobility model (described in the SI),^[44,60] where μ_{del} is the delocalized-state mobility of the initially formed large polaron, k_{loc} is the localization constant, μ_{loc} is the localized-state mobility (i.e., small polaron mobility), and k_1 is the recombination

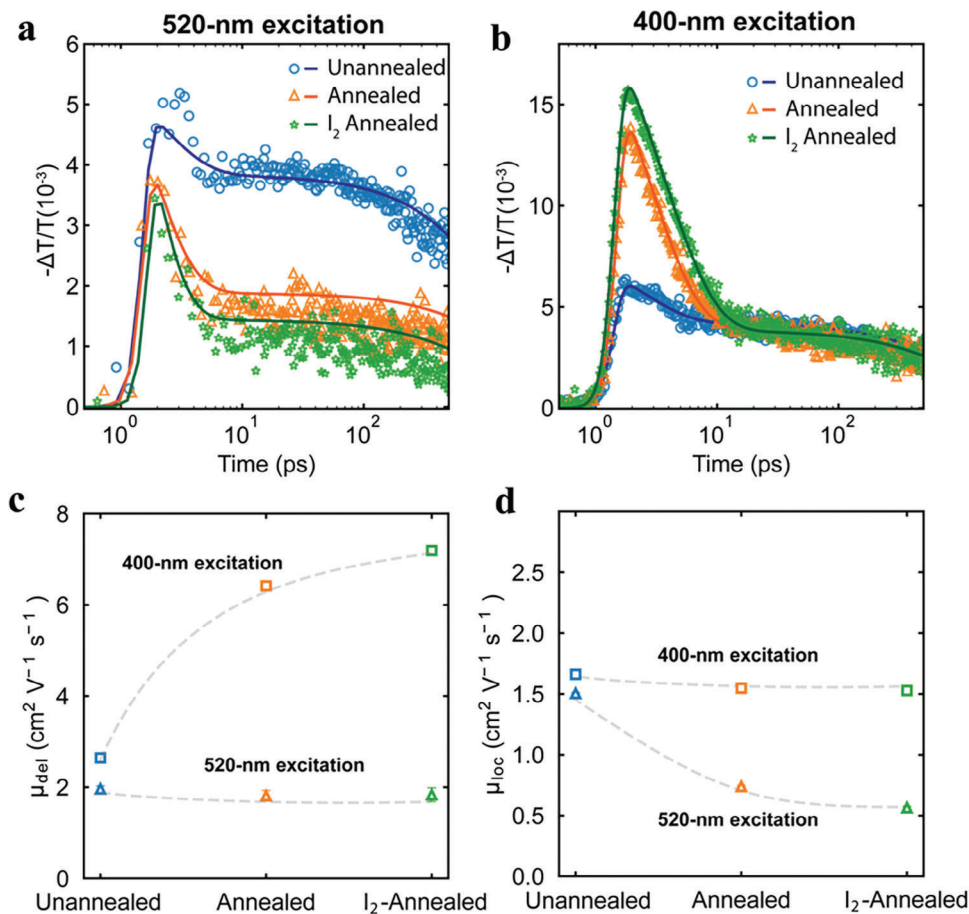


Figure 3. OPTP transients for unannealed (blue circles), air-annealed (orange triangles), and I_2 -annealed (green stars) Cu_2AgBiI_6 thin films after a) 520 nm and b) 400 nm pulsed excitation at a fluence of $65 \mu J cm^{-2}$. Markers represent experimental data, and solid lines represent fits to the two-level mobility model described in the Supporting Information. Effective THz charge-carrier mobilities for c) the delocalized state and d) the localized state in Cu_2AgBiI_6 thin films with different annealing conditions, extracted from two-level mobility model fitting to photoconductivity transients. Colored squares represent mobility values extracted for 400 nm excitation, while colored triangles represent mobility values extracted for 520 nm excitation. Dashed lines are guides to the eye.

constant of the localized state. As shown in Figure S11, Supporting Information, the two-level mobility model provides an excellent fit to the fluence-dependent OPTP data for all the studied thin films recorded under different excitation wavelengths. However, we note that the presence of CuI impurities and their possible influence on the photoconductivity complicates the interpretation of the extracted parameters (see detailed discussion in the SI).

Briefly, when comparing photoconductivity transients obtained following different excitation wavelengths (Figure S12, Supporting Information), we observe that 400 nm excitation systematically yields higher initial photoconductivity values, and that this increased photoconductivity is more marked and extends over longer times for both air- and I_2 -annealed thin films. These qualitative trends are confirmed by the parameters extracted from the above-mentioned two-level mobility model fitting (Figure 3c,d, and Tables S4 and S5, Supporting Information). We observe that, while slightly decreasing for direct Cu_2AgBiI_6 excitation, the initial delocalized-state mobility measured under 400 nm excitation conditions increases from $\epsilon_{del} = 2.6 \pm$

$0.1 cm^2 V^{-1} s^{-1}$ for the unannealed sample to $\epsilon_{del} = 7.2 \pm 0.4 cm^2 V^{-1} s^{-1}$ for I_2 -annealed thin films. On the other hand, the localized-state mobility is found to be constant around $\mu_{loc} \approx 1.5 cm^2 V^{-1} s^{-1}$ for 400 nm excitation.

As described in detail in the SI, we ascribe the high observed value for μ_{del} following 400 nm excitation to photoconductivity contributions from the CuI domains. To corroborate this hypothesis, we measured the photoconductivity transients in neat CuI thin films under similar excitation conditions (Figure S13, Supporting Information). The resulting high charge-carrier mobility for CuI thin films of $\mu_{CuI} \approx 16 cm^2 V^{-1} s^{-1}$ suggests that the high μ_{del} values obtained for nominal Cu_2AgBiI_6 films under 400 nm excitation conditions include contributions from charge carriers in both CuI and Cu_2AgBiI_6 to the photoconductivity signal. Here, we note that charge-carrier recombination in CuI is faster than in Cu_2AgBiI_6 as confirmed by the observed recombination rate for CuI $k_{CuI} \approx 0.2 ps^{-1}$. Therefore, charge carriers generated in CuI will quickly recombine or be funneled to the Cu_2AgBiI_6 phase (as predicted by the band alignment shown in Figure 2b), thus giving photoconductivity traces

representative of charge-carrier transport in the $\text{Cu}_2\text{AgBiI}_6$ phase at longer times.

The effect of CuI on charge-carrier transport in $\text{Cu}_2\text{AgBiI}_6$ thin films can be selectively studied by analyzing OPTP transients following 520 nm excitation, which will only excite the $\text{Cu}_2\text{AgBiI}_6$ directly and does not result in a direct injection of charge-carriers into CuI, although it is possible that holes may transfer. As shown in Figure 3a, we observe that the initial photoconductivity signal from $\text{Cu}_2\text{AgBiI}_6$ is only slightly affected by the increasing presence of CuI domains. We postulate that this marginal reduction of initial photoconductivity following 520 nm excitation is caused by the increased charge-carrier scattering arising from CuI domains distributed throughout the film, yielding slightly lower charge-carrier mobilities (Figure 3c).

On the other hand, we observe more pronounced photoconductivity decay dynamics for both air- and I_2 -annealed thin films with respect to unannealed $\text{Cu}_2\text{AgBiI}_6$ thin films. As described above and discussed more in detail by Buizza et al.,^[44,60] the formation of small polarons (i.e., the charge-carrier localization) yields a reduced charge-carrier mobility, resulting in a fast decay of the photoconductivity. Even though such fast decay is observed for unannealed thin films and is well captured by the two-level mobility model, we observe a comparatively faster and more pronounced decay dynamics for air- and I_2 -annealed $\text{Cu}_2\text{AgBiI}_6$ thin films (Figure 3a). These faster dynamics suggest that additional decay channels are introduced as a result of CuI domain formation. Interestingly, no such effect is observed when comparing 400 nm excited photoconductivity transients for the different thin films (Figure 3b). To reconcile these observations, we propose here that charge-carrier trapping at CuI domains causes faster photoconductivity decay dynamics for annealed $\text{Cu}_2\text{AgBiI}_6$ thin films, and that trap-filling mitigates this effect under 400 nm excitation conditions. As discussed in the SI, we note that a similar conclusion can be reached based on the two-level mobility model fitting parameters (Figure 3c,d). Overall, these findings reveal that CuI domains hinder charge-carrier transport in $\text{Cu}_2\text{AgBiI}_6$ thin films, with far-reaching implications for potential device applications.

2.3. Devices

To assess the photovoltaic properties of evaporated $\text{Cu}_2\text{AgBiI}_6$ films, we fabricated “nip” planar heterojunction devices using compact SnO_2 (c- SnO_2) as the electron transport layer, unannealed and air-annealed evaporated $\text{Cu}_2\text{AgBiI}_6$ films as the absorber, and undoped PTAA as the hole transport layer with a corresponding device structure of ITO/c- SnO_2 / $\text{Cu}_2\text{AgBiI}_6$ /PTAA/Au. We did not make photovoltaic devices with I_2 -treated films because this post-deposition process generated additional CuI impurity domains and degraded the morphology. The full fabrication procedure is described in the Supporting Information. We characterized the photovoltaic cells under simulated “1 sun” irradiance (100 mWcm^{-2} with air-mass (AM)1.5 global spectrum). Scans are first measured from forward-bias to short-circuit, which we refer to as reverse, and back to forward-bias (referred to as forwards) at a scan rate of 61 mVs^{-1} . Our champion device was recorded for an unannealed $\text{Cu}_2\text{AgBiI}_6$ film. The forward-bias to short-circuit scan yields a

PCE of 0.43%, J_{sc} of 2.20 mAcm^{-2} , V_{oc} of 0.34 V, and FF of 0.58, with the reverse scan giving almost identical values (Figure S14a, Supporting Information). The maximum power point tracked efficiency of our champion device was 0.42%, measured at the maximum power point for a duration of 30 s. However, when collating the results of several batches, we find that annealed films are on average higher performing and more reproducible than unannealed films. We were not able to reproduce the high efficiency of the 0.43% with an unannealed film. To demonstrate the difference between unannealed and annealed films, we show performance statistics for a number of different cells in Figure S15, Supporting Information. This plot groups together several different batches with devices that have been fabricated under different conditions (e.g., annealing temperature, absorber thickness, and transport layers, and passivation), with the aim of highlighting the difference between unannealed and annealed devices. We have not separated the parameters due to their lack of individual impact on the photovoltaic performance and poor reproducibility, as described further below. The results show that annealed films yield better photovoltaic parameters on average, with the measured steady-state open-circuit voltage, short-circuit current density, fill factor, and PCE being greater for annealed films compared to unannealed films. The forward bias to short-circuit scan of our champion annealed device was recorded for a 130 °C annealed film, yielding a PCE of 0.26%, J_{sc} of 1.51 mAcm^{-2} , V_{oc} of 0.32 V, and FF of 0.55 (Figure 4a), with a closely corresponding maximum power point tracked efficiency of 0.25% (inset, Figure 4a). 150 °C annealed films perform worse than 130 °C annealed films. Our best 150 °C annealed device (Figure 4b) yields a PCE of 0.13%, J_{sc} of 1.20 mAcm^{-2} , V_{oc} of 0.29 V, and FF of 0.39 in the forward bias to short-circuit scan, and slightly higher values in the reverse scan (PCE of 0.16%, J_{sc} of 1.53 mAcm^{-2} , V_{oc} of 0.28 V, and FF of 0.38). The corresponding maximum power point tracked efficiency is 0.17% (inset, Figure 4b). We ascribe this to poorer thin film morphology with increased annealing temperatures, leading to excessive shunting. Despite these challenges, the characteristics of our champion devices are consistent with the PCEs currently reported in the literature for solution-processed samples employing a compact metal oxide as the electron transport layer.^[31,42]

Although we obtain modest open-circuit voltages, the photocurrent losses are overwhelmingly the limiting factor in evaporated $\text{Cu}_2\text{AgBiI}_6$ devices, which is also true for solution-processed $\text{Cu}_2\text{AgBiI}_6$. In our evaporated devices, these losses account for over 80% of the expected short-circuit current density as calculated according to integrating the solar spectrum up until the band gap of $\text{Cu}_2\text{AgBiI}_6$, which is particularly surprising considering the high absorption coefficient measured. To attempt to mitigate shunt pathways originating from pinholes in the $\text{Cu}_2\text{AgBiI}_6$ absorber layer, we deposited a very thin layer (0.1 mg mL^{-1} in IPA) of insulating PMMA onto unannealed and annealed $\text{Cu}_2\text{AgBiI}_6$ samples before depositing the hole-transport layer, but this did not improve devices. Replacing PTAA with Spiro-OMeTAD did not improve devices either, nor did fabricate $\text{Cu}_2\text{AgBiI}_6$ devices with an active layer ranging from 60–400 nm, or changing the device architecture to the inverted “pin” structure. We, therefore, perceive that there is a major limitation of charge transport within the $\text{Cu}_2\text{AgBiI}_6$ absorber layer, rather than

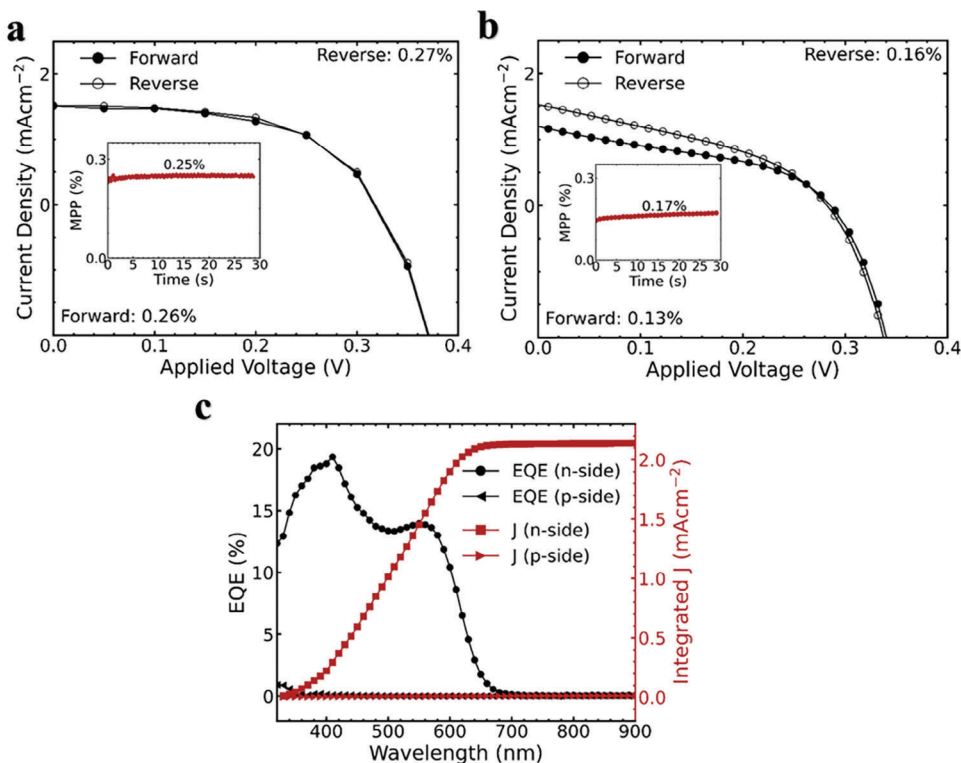


Figure 4. Forward (short-circuit to forward-bias) and reverse (forward-bias to short-circuit) current-voltage characteristics for the champion a) ITO/SnO₂/130 °C annealed Cu₂AgBiI₆/PTAA/Au and b) ITO/SnO₂/150 °C annealed Cu₂AgBiI₆/PTAA/Au devices. The steady-state PCE at the maximum power point is shown in the inset graph. c) External quantum efficiency measurements for front (n-side (glass)) and back (p-side (Ag)) illumination of 150 °C annealed semi-transparent ITO/c-SnO₂/Cu₂AgBiI₆/PTAA/MoO_x/ITO/Ag devices.

the relatively poor performance originating from non-optimal selection of device architecture or contact materials.

To understand the origin of these losses, we investigate the photocurrent generation and extraction in devices. We first created semi-transparent Cu₂AgBiI₆ devices by replacing the Au top electrode with MoO_x, semi-transparent indium tin oxide (ITO), and Ag ring contacts, giving the device structure of ITO/c-SnO₂/Cu₂AgBiI₆/PTAA/MoO_x/ITO/Ag (Figure S2a, Supporting Information). For the Cu₂AgBiI₆ films, we deposited 110 nm in thickness, and compared unannealed and annealed films, illuminated from the front (n-side (glass)) and back (p-side (contacts)), and measured the external quantum efficiency (EQE) to assess the efficiency of electron and hole transport. This technique considers that the density of electron-hole generation at a given point in the film is proportional to the number of photons absorbed at that point. Since the incident photons are attenuated exponentially according to the Beer-Lambert law, a higher density of electron-hole pairs is generated closest to the illuminated transport layer. Therefore, when the n-side is illuminated first, electrons have to travel the least distance to reach the c-SnO₂ layer, whilst holes have to travel further to the rear contact. Conversely, when the p-side is illuminated, electrons have the furthest to travel to be extracted by the ETL, whilst holes have the least distance to traverse. The EQE results for unannealed and 150 °C air-annealed films are shown in Figure S14b, Supporting Information and Figure 4c respectively. The current-voltage characterization of the devices used for EQE measurements is shown

in Figure S16, Supporting Information. Unannealed films, regardless of illumination side, show almost zero extraction efficiency. When illuminating 150 °C air-annealed films from the n-side, the EQE (red line) spectra closely follow the absorption spectra presented in Figure 2c, and have an integrated current density of 2.25 mAcm⁻², consistent with J_{sc} measured in devices. The EQE onset at ≈700 nm, which peaks at 15%, can be assigned to photon absorption from Cu₂AgBiI₆, whilst the EQE peak of 20% at ≈417 nm, can be ascribed to a mixture of CuI and Cu₂AgBiI₆ domains. When illuminated from the p-side, we measure almost no EQE (blue line) and hence integrated current density, indicating loss of the initially high photo-generated carrier density. This finding highlights an imbalance in the charge extraction efficiency of electrons and holes in the device. Considering EQE is smallest when illuminating from the p-side, and hence when electrons have the greatest distance to travel, we conclude that electron diffusion is the overriding factor limiting charge extraction in Cu₂AgBiI₆ devices, similar to reports on the double perovskite, Cs₂AgBiBr₆.^[16]

3. Discussion

The presence of CuI and its impacts on the excited state dynamics of Cu₂AgBiI₆ thin films are demonstrated here by combining absorption, PL, and OPTP spectroscopy measurements. Crucially, PL and OPTP measurements indicate that CuI impurities are not benign, but rather significantly interact with charge carriers

in $\text{Cu}_2\text{AgBiI}_6$ and account for the photoluminescence properties of the thin films. The community currently uses PL and TRPL as metrics to assess radiative efficiency and photo-generated carrier lifetime, respectively. However, we note the emergence of the role played by CuI in this material imposes a reconsideration of this approach for $\text{Cu}_2\text{AgBiI}_6$ and other related compounds. The PL emission at 730 nm is ascribed here to an iodine defect-mediated transition in CuI domains. Therefore, any measured lifetime, or properties involving lifetime, such as diffusion length, associated with this emission peak is likely reflective of trapped charges in CuI domains, not free-carriers in $\text{Cu}_2\text{AgBiI}_6$, highlighting the need to exercise caution when assessing apparent improvements in $\text{Cu}_2\text{AgBiI}_6$ optoelectronic properties using conventional indicators. This finding is also relevant to solution-processed $\text{Cu}_2\text{AgBiI}_6$ materials with similar absorption and PL characteristics. We observed that annealing in I_2 rich atmosphere does not quench the defect-emission. Surprisingly, it has the opposite effect. We observe from XRD and absorption measurements that annealing in I_2 vapor induces more CuI formation, which results in increased photoluminescence intensity from the CuI defect transition.

Our OPTP transient conductivity spectroscopy results indicate that, although the direct photoexcitation of CuI domains yields high early-time photoconductivity, charge carriers are funneled from CuI to $\text{Cu}_2\text{AgBiI}_6$ and rapidly localize. On the other hand, charge-carriers in the $\text{Cu}_2\text{AgBiI}_6$ phase interact with these CuI domains (e.g., via ultrafast trapping), yet still exhibit considerable charge-carrier mobility, with the unannealed films exhibiting the highest later-time mobility. In light of this, future work should be directed toward achieving phase purity (e.g., eliminating the CuI impurities). However, this is a challenge for the $\text{Cu}_2\text{AgBiI}_6$ phase space where composition-temperature sensitivity is reported across a number of synthesis pathways. For example, in the powder synthesis of $\text{Cu}_2\text{AgBiI}_6$, slowly cooling leads to a distribution of compositions, whilst synthesizing at, and rapidly quenching from 350 °C produces compositionally homogenous powder.^[31] XRD data can often also appear to originate from a single phase, but the close overlap in XRD peaks of many closely related compounds, e.g., CuAgBiI_5 , Cu_2BiI_5 , $\text{Ag}_x\text{Bi}_y\text{I}_{x+3y}$, and CuI means often there is some level of uncertainty surrounding phase constitution, which could be due to the complex phase-space and phase diagrams associated with $\text{Cu}_2\text{AgBiI}_6$ and Ag-Bi-I respectively, originating from the general disorder and the cubic-close packed iodide sublattice underpinning their structures. Thus, phases made at high temperature via solid-state techniques are not necessarily the phases formed at low temperature from thin-film processing techniques, and therefore it may be possible to find a more ordered room-temperature Cu-Ag-Bi-I phase beyond $\text{Cu}_2\text{AgBiI}_6$ and CuAgBiI_5 . Assessing our own film processing conditions, no intentional substrate heating was applied to evaporated films. However, by measuring the substrate temperature using non-electronic temperature indicators, we find our samples reached a temperature of 60 °C during deposition due to heating from the thermal sources. Measuring this way meant we were only able to record the maximum substrate temperature, but we expected it to evolve during film deposition and cooling. This is likely a significant variable determining the phase of unannealed films, which then forms the base template for all annealed films. Controlling the substrate tem-

perature during deposition and cooling could therefore be important in controlling the phase and morphology of evaporated $\text{Cu}_2\text{AgBiI}_6$.

Compared to unannealed films, devices using an annealed $\text{Cu}_2\text{AgBiI}_6$ absorber layer on average have higher open-circuit voltage, short-circuit current density, fill factor, PCE, and EQE, with 130 °C annealed $\text{Cu}_2\text{AgBiI}_6$ devices performing better than films annealed at 150 °C, likely because of the increased density of pinholes found in 150 °C annealed films. Through front-side and rear-side illumination studies, we demonstrated that poor transport of electrons, as opposed to holes, through the $\text{Cu}_2\text{AgBiI}_6$ films is responsible for the very low short-circuit current densities. From the measured optoelectronic and morphological properties, we would have expected the unannealed films to perform better than the annealed films in solar cells. This only occurred in one instance, however. In all other batches, the unannealed films performed extremely poorly in devices. We postulate that this is caused by the increased unintentional charge-carrier density in the unannealed films, which is presumably a p-type majority carrier since hole transport appears favorable, resulting in even shorter diffusion lengths for electrons as a result of increased minority charge-carrier recombination rates. Considering the imbalance of electron and hole extraction, the prominent defects are likely to be electron traps. For example, iodine vacancies have been found to have a low formation energy in $\text{Cu}_2\text{AgBiI}_6$ due to the presence of bismuth.^[40] Therefore, substituting bismuth in evaporated films presents an opportunity to reduce trap density and enhance device performance, mirroring the success seen in solution-processed $\text{Cu}_2\text{AgBiI}_6$ films.^[40] Annealing co-evaporated films at lower temperatures, or sequential deposition, could also help modify the crystallization process to suppress the formation of CuI whilst effectively reducing intrinsic defects.

4. Conclusion

In summary, our study successfully demonstrates the viability of co-evaporation as a promising technique for fabricating quaternary $\text{Cu}_2\text{AgBiI}_6$ films for use in solar cells, achieving modest PCEs using a planar electron transport layer. In particular, we unravel the significant impact of CuI impurities on $\text{Cu}_2\text{AgBiI}_6$ films, attributing the PL emission at 730 nm to defect-mediated transitions within CuI impurity domains. The presence of CuI also influences the excited-state dynamics of $\text{Cu}_2\text{AgBiI}_6$ thin films, leading to faster charge localization and reduced long-time photoconductivity compared to films with less CuI present. Furthermore, our investigation reveals an imbalance in electron and hole diffusion lengths, which is a significant factor limiting the efficiency of photovoltaic devices. By optimizing the deposition process to suppress CuI formation and identifying the source of electron traps, we expect significant improvements in the performance of $\text{Cu}_2\text{AgBiI}_6$ -based solar cells.

Supporting Information

Supporting Information is available from the Wiley Online Library or from the author.

Acknowledgements

This work was partly funded by the Engineering and Physical Sciences Research Council (EPSRC) UK, under grants EP/V010840/1 and EP/S004947/1. B.W.J.P. would like to thank the Penrose Scholarship for generously funding his studentship. The author would also like to thank Moorfield Nanotechnology for custom designing and manufacturing the co-deposition system used in this study, and for their expert assistance, as well as Kratos Analytical for their UPS measurements. H.J. acknowledges the support of the sponsorships from Oxford PV. A.J.R. acknowledges the support of the EU Horizon grant, no. 861985 (PeroCUBE). L.M.H. acknowledges support through a Hans Fischer Senior Fellowship from the Technical University of Munich's Institute for Advanced Study, funded by the German Excellence Initiative.

Conflict of Interest

H.J.S. is co-founder and CSO of Oxford PV Ltd., a company commercializing perovskite PV technology.

Data Availability Statement

The data that support the findings of this study are available from the corresponding author upon reasonable request.

Keywords

co-evaporation, Cul domains, electron-diffusion length, I₂-annealing, spectroscopy

Received: October 2, 2023
Revised: December 11, 2023
Published online:

- [1] M. D. Bastiani, V. Larini, R. Montecucco, G. Grancini, *Energy Environ. Sci.* **2023**, *16*, 421.
- [2] Z. Li, Y. Zhao, X. Wang, Y. Sun, Z. Zhao, Y. Li, H. Zhou, Q. Chen, *Joule* **2018**, *2*, 1559.
- [3] Z. J. Yu, J. V. Carpenter, Z. C. Holman, *Nat. Energy* **2018**, *3*, 747.
- [4] M. T. Hörantner, T. Leijtens, M. E. Ziffer, G. E. Eperon, M. G. Christoforo, M. D. McGehee, H. J. Snaith, *ACS Energy Lett.* **2017**, *2*, 2506.
- [5] D. P. Mcmeekin, G. Sadoughi, W. Rehman, G. E. Eperon, M. Saliba, M. T. Hörantner, A. Haghighirad, N. Sakai, L. Korte, B. Rech, M. B. Johnston, L. M. Herz, H. J. Snaith, *Science* **2016**, *351*, 151.
- [6] M. A. Green, A. Ho-Baillie, H. J. Snaith, *Nat. Photonics* **2014**, *8*, 506.
- [7] S. D. Stranks, G. E. Eperon, G. Grancini, C. Menelaou, M. J. P. Alcocer, T. Leijtens, L. M. Herz, A. Petrozza, H. J. Snaith, *Science* **2013**, *342*, 341.
- [8] C. Wehrenfennig, G. E. Eperon, M. B. Johnston, H. J. Snaith, L. M. Herz, *Adv. Mater.* **2014**, *26*, 1584.
- [9] A. J. Knight, J. Borchert, R. D. J. Oliver, J. B. Patel, P. G. Radaelli, H. J. Snaith, M. B. Johnston, L. M. Herz, *ACS Energy Lett.* **2021**, *6*, 799.
- [10] A. J. Knight, A. D. Wright, J. B. Patel, D. P. Mcmeekin, H. J. Snaith, M. B. Johnston, L. M. Herz, *ACS Energy Lett.* **2019**, *4*, 75.
- [11] E. J. Juarez-Perez, L. K. Ono, Y. Qi, *J. Mater. Chem. A* **2019**, *7*, 16912.
- [12] A. Senocrate, G. Y. Kim, M. Grätzel, J. Maier, *ACS Energy Lett.* **2019**, *4*, 2859.
- [13] M. Delor, A. H. Slavney, N. R. Wolf, M. R. Filip, J. B. Neaton, H. I. Karunadasa, N. S. Ginsberg, *ACS Energy Lett.* **2020**, *5*, 1337.
- [14] R. L. Z. Hoye, L. Eyre, F. Wei, F. Brivio, A. Sadhanala, S. Sun, W. Li, K. H. L. Zhang, J. L. Macmanus-Driscoll, P. D. Bristowe, R. H. Friend, A. K. Cheetham, F. Deschler, *Adv. Mater. Interfaces* **2018**, *5*, 1800464.
- [15] N. K. Tailor, A. Listorti, S. Colella, S. Satapathi, *Adv. Mater. Technol.* **2023**, *8*, 2200442.
- [16] G. Longo, S. Mahesh, L. R. V. Buizza, A. D. Wright, A. J. Ramadan, M. Abdi-Jalebi, P. K. Nayak, L. M. Herz, H. J. Snaith, *ACS Energy Lett.* **2020**, *5*, 2200.
- [17] A. H. Slavney, T. Hu, A. M. Lindenberg, H. I. Karunadasa, *J. Am. Chem. Soc.* **2016**, *138*, 2138.
- [18] M. R. Filip, S. Hillman, A. A. Haghighirad, H. J. Snaith, F. Giustino, *J. Phys. Chem. Lett.* **2016**, *7*, 2579.
- [19] E. T. McClure, M. R. Ball, W. Windl, P. M. Woodward, *Chem. Mater.* **2016**, *28*, 1348.
- [20] M. Khazaei, K. Sardashti, C.-C. Chung, J.-P. Sun, H. Zhou, E. Bergmann, W. A. Dunlap-Shohl, Q. Han, I. G. Hill, J. L. Jones, D. C. Lupascu, D. B. Mitzi, *J. Mater. Chem. A* **2019**, *7*, 2095.
- [21] H. C. Sansom, G. F. S. Whitehead, M. S. Dyer, M. Zanella, T. D. Manning, M. J. Pitcher, T. J. Whittles, V. R. Dhanak, J. Alaria, J. B. Claridge, M. J. Rosseinsky, *Chem. Mater.* **2017**, *29*, 1538.
- [22] K. W. Jung, M. R. Sohn, H. M. Lee, I. S. Yang, S. D. Sung, J. Kim, E. Wei-Guang Diao, W. I. Lee, *Sustainable Energy Fuels* **2017**, *2*, 294.
- [23] Q. Zhang, C. Wu, X. Qi, F. Lv, Z. Zhang, Y. Liu, S. Wang, B. Qu, Z. Chen, L. Xiao, *ACS Appl. Energy Mater.* **2019**, *2*, 3651.
- [24] H. Wu, H. Zhu, A. Erbing, M. B. Johansson, S. Mukherjee, G. J. Man, H. Rensmo, M. Odellius, E. M. J. Johansson, *ACS Appl. Energy Mater.* **2019**, *2*, 5356.
- [25] N. Pai, J. Lu, T. R. Gengenbach, A. Seeber, A. S. R. Chesman, L. Jiang, D. C. Senevirathna, P. C. Andrews, U. Bach, Y.-B. Cheng, A. N. Simonov, *Adv. Energy Mater.* **2018**, *9*, 1803396.
- [26] Z. Shao, T. Le Mercier, M. B. Madec, T. Pauporté, *Mater. Lett.* **2018**, *221*, 135.
- [27] B. Ghosh, B. Wu, X. Guo, P. C. Harikesh, R. A. John, T. Baikie, Arramel, A. T. S. Wee, C. Guet, T. C. Sum, S. Mhaisalkar, N. Mathews, *Adv. Energy Mater.* **2018**, *8*, 1802051.
- [28] C. Lu, J. Zhang, H. Sun, D. Hou, X. Gan, M.-H. Shang, Y. Li, Z. Hu, Y. Zhu, L. Han, *ACS Appl. Energy Mater.* **2018**, *1*, 4485.
- [29] H. Zhu, M. Pan, M. B. Johansson, E. M. J. Johansson, *ChemSusChem* **2017**, *10*, 2592.
- [30] A. Kulkarni, F. Ünlü, N. Pant, J. Kaur, C. Bohr, A. K. Jena, S. Öz, M. Yanagida, Y. Shirai, M. Ikegami, K. Miyano, Y. Tachibana, S. Chakraborty, S. Mathur, T. Miyasaka, *Sol. RRL* **2021**, *5*, 2100077.
- [31] H. C. Sansom, G. Longo, A. D. Wright, L. R. V. Buizza, S. Mahesh, B. Wenger, M. Zanella, M. Abdi-Jalebi, M. J. Pitcher, M. S. Dyer, T. D. Manning, R. H. Friend, L. M. Herz, H. J. Snaith, J. B. Claridge, M. J. Rosseinsky, *J. Am. Chem. Soc.* **2021**, *143*, 3983.
- [32] Z. Xiao, W. Meng, J. Wang, D. B. Mitzi, Y. Yan, *Mater. Horiz.* **2017**, *4*, 206.
- [33] L. R. V. Buizza, H. C. Sansom, A. D. Wright, A. M. Ulatowski, M. B. Johnston, H. J. Snaith, L. M. Herz, *Adv. Funct. Mater.* **2022**, *32*, 2108392.
- [34] W. Zhang, J. Smith, R. Hamilton, M. Heaney, J. Kirkpatrick, K. Song, S. E. Watkins, T. Anthopoulos, I. McCulloch, *J. Am. Chem. Soc.* **2009**, *131*, 10814.
- [35] A. K. Jena, A. Kulkarni, T. Miyasaka, *Chem. Rev.* **2019**, *119*, 3036.
- [36] H. Park, R. Chaurasiya, B. H. Jeong, P. Sakhivel, H. J. Park, *Adv. Photonics Res.* **2021**, *2*, 2000178.
- [37] Y. Seo, S. R. Ha, S. Yoon, S. M. Jeong, H. Choi, D.-W. Kang, *J. Power Sources* **2020**, *453*, 227903.
- [38] F. Zhang, Z. Hu, B. Zhang, Z. Lin, J. Zhang, J. Chang, Y. Hao, *ACS Appl. Mater. Interfaces* **2022**, *14*, 18498.
- [39] G. K. Grandhi, B. Al-Anesi, H. Pasanen, H. Ali-Löytty, K. Lahtonen, S. Granroth, N. Christian, A. Matuhina, M. Liu, A. Berdin, V. Pecunia, P. Vivo, *Small* **2022**, *18*, 2203768.

- [40] B. Al-Anesi, G. K. Grandhi, A. Pecoraro, V. Sugathan, N. S. M. Viswanath, H. Ali-Löyty, M. Liu, T.-P. Ruoko, K. Lahtonen, D. Manna, S. Toikkonen, A. B. Muñoz-García, M. Pavone, P. Vivo, *Small* **2023**, 19, 2303575.
- [41] G. Krishnamurthy Grandhi, S. Toikkonen, B. Al-Anesi, V. Pecunia, P. Vivo, *Sustainable Energy Fuels* **2023**, 7, 66.
- [42] N. Pai, M. Chatti, S. O. Furer, A. D. Scully, S. R. Raga, N. Rai, B. Tan, A. S. R. Chesman, Z. Xu, K. J. Rietwyk, S. S. Reddy, Y. Hora, G. A. Sepalage, N. Glück, M. Lira-Cantú, U. Bach, A. N. Simonov, *Adv. Energy Mater.* **2022**, 12, 2201482.
- [43] H. C. Sansom, L. R. V. Buizza, M. Zanella, J. T. Gibbon, M. J. Pitcher, M. S. Dyer, T. D. Manning, V. R. Dhanak, L. M. Herz, H. J. Snaith, J. B. Claridge, M. J. Rosseinsky, *Inorg. Chem.* **2021**, 60, 18154.
- [44] L. R. V. Buizza, A. D. Wright, G. Longo, H. C. Sansom, C. Q. Xia, M. J. Rosseinsky, M. B. Johnston, H. J. Snaith, L. M. Herz, *ACS Energy Lett.* **2021**, 6, 1729.
- [45] J. Li, H. Wang, X. Y. Chin, H. A. Dewi, K. Vergeer, T. W. Goh, J. W. M. Lim, J. H. Lew, K. P. Loh, C. Soci, T. C. Sum, H. J. Bolink, N. Mathews, S. Mhaisalkar, A. Bruno, *Joule* **2020**, 4, 1035.
- [46] Y. Duan, G. Zhao, X. Liu, J. Ma, S. Chen, Y. Song, X. Pi, X. Yu, D. Yang, Y. Zhang, F. Guo, *Appl. Surf. Sci.* **2021**, 562, 150153.
- [47] R. Kurdyumova, R. Baranova, *Kristallografiya* **1961**, 6, 402.
- [48] W. Sun, H. Peng, Y. Li, W. Yan, Z. Liu, Z. Bian, C. Huang, *J. Phys. Chem. C* **2014**, 118, 16806.
- [49] S. Rai, B. K. Pandey, A. Garg, D. K. Dwivedi, *Opt. Mater.* **2021**, 121, 111645.
- [50] L. J. van der Pauw, *Philips Res. Rep.* **1958**, 13, 01.
- [51] F. Peña-Camargo, M. Stolterfoht, H. Hempel, A. Musiienko, V. M. Le Corre, J. Thiesbrummel, J. Warby, T. Unold, F. Lang, D. Neher, J. Diekmann, presented at Proc. of the Int. Conf. on Hybrid and Organic Photovoltaics, València, May, **2022**.
- [52] R. J. Elliott, *Phys. Rev.* **1957**, 108, 1384.
- [53] J.-H. Cha, D.-Y. Jung, *ACS Appl. Mater. Interfaces* **2017**, 9, 43807.
- [54] A. Das, K. Pal, P. Acharyya, S. Das, K. Maji, K. Biswas, *J. Am. Chem. Soc.* **2023**, 145, 1349.
- [55] G. Lin, F. Zhao, Y. Zhao, D. Zhang, L. Yang, X. Xue, X. Wang, C. Qu, Q. Li, L. Zhang, *Materials* **2016**, 9, 990.
- [56] O. Madkhali, M. Jullien, A. E. Giba, J. Ghanbaja, S. Mathieu, C. Gendarme, S. Migot, Y. Alajlani, N. Can, F. Alnjiman, D. Horwat, A. Redjaimia, J. F. Pierson, *Surf. Interfaces* **2021**, 27, 101500.
- [57] W. Yu, G. Benndorf, Y. Jiang, K. Jiang, C. Yang, M. Lorenz, M. Grundmann, *Phys. Status Solidi RRL* **2021**, 15, 2000431.
- [58] A. Liu, H. Zhu, M.-G. Kim, J. Kim, Y.-Y. Noh, *Adv. Sci.* **2021**, 8, 2100546.
- [59] K. Gotoh, M. Cui, I. Takahashi, Y. Kurokawa, N. Usami, *Energy Procedia* **2017**, 124, 598.
- [60] A. D. Wright, L. R. V. Buizza, K. J. Savill, G. Longo, H. J. Snaith, M. B. Johnston, L. M. Herz, *J. Phys. Chem. Lett.* **2021**, 12, 3352.